View Article Online
View Journal

Journal of Materials Chemistry A

Materials for energy and sustainability

Accepted Manuscript

This article can be cited before page numbers have been issued, to do this please use: K. SEKAR, C. Chuaicham, R. Pawar, K. Sasaki, W. Li, A. F. Lee and K. Wilson, *J. Mater. Chem. A*, 2019, DOI: 10.1039/C9TA07009E.

ROYAL SOCIETY OF CHEMISTRY

rsc.li/materials-a

View Article Online
DOI: 10.1039/C9TA07009E

Template free mild hydrothermal synthesis of core-shell Cu_2O(Cu)@CuO visible light photocatalysts for N-acetyl-para-aminophenol degradation

Sekar Karthikeyan,[†] Chitiphon Chuaicham,[†] Radheshyam R Pawar,[†] Keiko Sasaki,[†*] Wei Li,[‡] Adam F. Lee,[‖*] Karen Wilson[‖]

[†]Department of Earth Resources Engineering, Faculty of Engineering, Kyushu University, 744 Motooka, Nishiku, Fukuoka 819-0395, Japan

[‡]European Bioenergy Research Institute, Aston Institute of Materials Research, Aston University, Birmingham B4 7ET, UK

[‖]Applied Chemistry & Environmental Science, RMIT University, Melbourne VIC 3000, Australia.

*Corresponding Author: E-mail: keikos@mine.kyushu-u.ac.jp, adam.lee2@rmit.edu.au ; Tel: +81-92-802-3338, +61 399252623

Abstract

Solar photocatalytic processes are a promising approach to environmental remediation, however their implementation requires improvements in visible light harvesting and conversion and a focus on low cost, Earth abundant materials. Semiconducting copper oxides are promising visible light photocatalysts for solar fuels and wastewater depollution. Here we report the mild, hydrothermal (template-free) synthesis of core-shell Cu_2O(Cu)@CuO photocatalytic architectures for the visible light photocatalytic degradation of N-acetyl-para-aminophenol (APAP). Hollow and rattle-like core-shell nanosphere aggregates with diameters between 200 nm and 2.5 μm formed under different synthesis conditions; all comprised an inner Cu_2O shell, formed of 10-50 nm nanoparticles, surrounded by a protective corona of CuO nanoparticles. High reductant and structure-directing agent concentrations promoted the formation of a yolk-like Cu_2O/Cu core, associated with improved photophysical properties, notably a high oxidation potential and suppressed charge carrier recombination, that correlated with the highest apparent quantum efficiency (8 %) and rate of APAP removal (7 $\mu mol.g^{-1}.min^{-1}$). Trapping experiments demonstrated hydroxyl radicals were the primary active species responsible for APAP oxidation to quinones and short chain carboxylic acids. Rattle-like core-shell Cu_2O/Cu@CuO nanospheres exhibited excellent physiochemical stability and recyclability for APAP photocatalytic degradation.

Keywords: *Photocatalysis; copper; core-shell nanoparticles; N-acetyl-para-aminophenol; depollution*

1. Introduction

Solar energy utilisation by semiconductor nanomaterials is the subject of intensive fundamental research and technological developments for applications in environmental remediation,[1] and fuels[2] and fine chemicals[3, 4] production. Titania has been the inorganic semiconductor photocatalyst of choice for hydrogen production,

View Article Online
DOI: 10.1039/C9TA07009E

wastewater treatment, pathogen inactivation, and in personal care products,[5, 6] however as a wide band gap (>3.2 eV) semiconductor it can only absorb up to 5 % of sunlight reaching the Earth's surface.[7] Cuprous oxide (Cu_2O) is a low cost and Earth abundant p-type narrow band gap (2.0 to 2.5 eV) semiconductor, with conduction and valence band energies suited to visible light driven for solar fuels production, water splitting and environmental depollution.[8] Various strategies have been adopted to engineer the photophysical properties of Cu_2O nanomaterials through controlling their size,[9] morphology[10] and surface termination,[11, 12] and the introduction of co-catalysts[13] and heterojunctions,[14] with the goal of improved light absorption and photoexcited charge carrier lifetimes (and consequently quantum efficiency) in addition to enhanced photocatalytic stability.[15] Cu_2O nanostructures can exhibit unexpected photophysics, for example charge separation across the surface of cubic Cu_2O single crystal photocatalysts induced by asymmetric illumination; visible light excited holes (h+) and electrons (e-) migrate to illuminated and shadowed regions respectively as a result of different charge carrier mobilities.[16] Cupric oxide (CuO, band gap 1.2 to 1.7 eV) has also been used as a co-catalyst to stabilise Cu_2O and affect charge separation across heterojunction interfaces.[17-19] Diverse Cu_2O composite nanostructures are reported, enabling tuning of textural, electronic, and optical properties for thermal, photo- and electrocatalysis.[20-22] Among these, are core-shell/hollow Cu/Cu_2O and CuO/Cu_2O architectures, synthesised by low (230 nm to 260 nm single crystal Cu_2O hollow spheres)[23] or high temperature (4-10 nm single crystal Cu_2O@CuO nanoparticles)[24] surfactant templating, or templateless high temperature(<450 °C),[25, 26] electrodeposition,[17, 27] solvothermal,[20, 28] or hydrothermal[29] processing. Yang et al report that Cu_2O/CuO bilayered composite photocathodes are advantageous for photoelectrochemical hydrogen evolution due to injection of photoexcited electrons from the Cu_2O conduction band (CB) to that of CuO and concomitant reverse injection of photoexcited holes from the CuO valence band (VB) to that of Cu_2O, increasing carrier transport rates through the composite and across the photocathode/solution interface.[17] However, core-shell/hollow CuO/Cu_2O architectures have rarely been applied to wastewater depollution, and only then for dye degradation[29] [25, 26] wherein photosensitisation is problematic.[30]

We recently reported the synthesis of hierarchical[31] and size controlled (50-500 nm) non-porous[9] Cu_2O nanocubes for photocatalytic H_2 production and phenol degradation respectively, and hence were curious to explore the potential of core-shell/hollow CuO_x systems for removing organic micropollutants from water.[32] N-acetyl-para-aminophenol (APAP) is an important nonsteroidal anti-inflammatory, analgesic and antipyretic drug that is extensively used in global healthcare, and a xenobiotic found in wastewater at ng.L^{-1} to μg.L^{-1} levels in ground and drinking water,[33] and whose long-term adverse effects on biological and pharmacokinetic activity are of significant concern. In Japan, levels as high as 92 μg.L^{-1} are reported in river water downstream of a hospital effluent sewage treatment plant,[33] while levels reached 65 μg.L^{-1} in the Tyne river (UK),[34] 6 μg.L^{-1} and 10 μg L^{-1} for sewage effluent in Europe and natural water in the USA respectively,[35] 0.033 and 6.8 μg.L^{-1} for surface and river water in South Korea.[36]

View Article Online
DOI: 10.1039/C9TA07009E

Here we describe the mild (60 °C) hydrothermal synthesis, characterisation and application of core-shell $Cu_2O(Cu)@CuO$ nanospheres with diameters between from 200 nm and 2 μm. Photophysical properties were investigated by bulk and surface analytical techniques including XRD, SEM, HR(S)TEM, XANES, XPS, N_2 porosimetry, and UV-visible spectroscopies. $Cu_2O(Cu)@CuO$ hollow nanospheres comprised shells of Cu_2O nanoparticle aggregates decorated by a CuO nanoparticulate corona, attributed to Ostwald ripening of Cu_2O nuclei during the reduction/ageing; high reductant and PEG concentrations also resulted in a rattle-like core of Cu_2O and Cu nanoparticles. The rattle-like core-shell $Cu_2O/Cu@CuO$ nanospheres exhibited the highest quantum efficiency and activity for visible light photocatalytic degradation of APAP by hydroxyl radicals, demonstrating potential use in wastewater treatment.

2. Experimental

2.1. Chemicals

Copper (II) chloride dihydrate ($CuCl_2.2H_2O$, Wako 99.9 %), polyethylene glycol (Wako 560-640 M.W.), sodium hydroxide (NaOH, Wako 98 %), hydrazine monohydrate ($H_4N_2.H_2O$, Wako 98 %), ethanol (Wako 99.5 %), acetonitrile (Wako 99.8 %), HPLC grade water (Wako), N-acetyl-para-aminophenol (i.e. Paracetamol or acetaminophen, TCI 98 %).

2.2. Core-shell $Cu_2O@CuO$ photocatalyst synthesis

A core-shell $Cu_2O@CuO$ photocatalyst was fabricated by a template-free hydrothermal method (**Scheme 1**). 50 mL of 0. 2 M copper chloride dihydrate and 3 mL of 0.01 M PEG-600 were added to a three neck round-bottomed flask along with 6 mL of water and stirred at 600 rpm at 60 °C for 5 min until a deep blue solution was obtained. Subsequently, 10 mL of 2 M NaOH and then 1 mL of 2 M hydrazine monohydrate with 10 mL of water were added dropwise to the preceding solution, and stirred for a further 15 min. The resulting mixture was transferred to a sealed round-bottomed flask under N_2 for 30 min to allow the formation of a yellowish-red Cu2O@CuO precipitate, which was then filtered and washed three times with water and three times with ethanol to ensure removal of residual PEG, centrifuged in a TOMY Suprema 21 high speed refrigerated centrifuge for 6 min at 10000 rpm, and then freeze dried in an EYELA Freeze Dryer FDU-2100 for 24 h. The resulting solid was stored in a desiccator and is termed $Cu_2O@CuO$-B. We believe that PEG complexes the initial Cu (II) ions and controls the morphology of mixed Cu (I/II) oxide nanostructures formed during subsequent NaOH/hydrazine induced (partial) reduction and precipitation according to **Eqn. 1.**

$$4CuCl_2 + N_2H_4.H_2O + 8NaOH \rightarrow 2Cu_2O + N_2 + 8NaCl + 7H_2O \qquad (1)$$

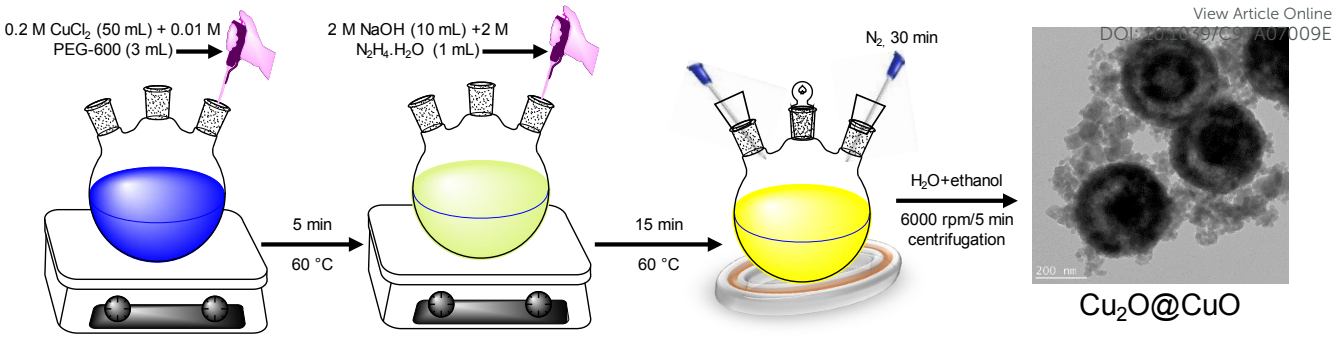

Scheme 1. Synthesis of core-shell Cu_2O@CuO photocatalysts.

Three related materials were also synthesised: Cu_2O@CuO-A in which 0.5 mL of 2 M hydrazine monohydrate volume was used; Cu_2O@CuO-C in which 10 mL of 2 M NaOH was added prior to the addition of 0.5 mL of 1 M hydrazine monohydrate; and Cu_2O@CuO-D adopting the same protocol as for Cu_2O-C but in which only 0.5 mL of PEG was used in the first step of the synthesis.

2.3. Catalyst characterisation

Photophysical properties of the four catalysts were characterized by bulk and surface analytical methods. Powder X-ray diffraction (PXRD) was performed using a Rigaku Ultima IV diffractometer with Cu K_α radiation at 40 kV/40 mA with a step size of 0.02°. Band gaps (Eg) were calculated by diffuse reflectance UV-Vis spectroscopy (DRUVS) on a Shimadzu UV-2450 spectrophotometer equipped with an ISR-2200 integrating sphere. Solid state photoluminescence spectroscopy (PL) was performed using a JASCO F-6600 spectrofluorometer. Transmission electron microscopy (TEM) imaging was conducted using a JEOL JEM-2100HCKM instrument, and field emission scanning electron microscopy (FE-SEM) imaging on a ZEISS ULTRA™ 55 (344999-9055-100) instrument. (S)TEM samples were prepared by dispersion in ethanol, sonication, drop casting on carbon coated copper grids (molybdenum grids were used for EDX elemental mapping using a JED-2300T detector) and drying. X-ray photoelectron spectra (XPS) were collected on an ULVAC-PHI ESCA 5800 spectrometer using a monochromated Al K_α X-ray source operated at 200 W. Energy referencing was performed using the C 1s peak for adventitious carbon set to 284.6 eV, and peak fitting was undertaken using Casa XPS Version 2.3.16. Specific surface area and pore size analysis was performed using a BEL-Max N_2 porosimeter on degassed samples. Cu K-edge XANES spectra of the as-prepared catalysts and Cu foil, Cu_2O and CuO reference materials were measured on BL15 of the Kyushu Synchrotron Light Research Center (SAGA-LS; Tosu, Japan) in transmission mode. Samples were prepared by dilution with BN and mounted with Kapton tape. The photon energy was scanned using a Si double crystal monochromator from 8.9 to 9.2 keV. The storage ring operating current was 171.9 mA at 1.40 GeV. Linear combination fitting (LCF) analysis was performed using the Athena-Demeter 0.9.26 program in the IFEFFIT software package.

View Article Online
DOI: 10.1039/C9TA07009E

2.4. N-acetyl-para-aminophenol (APAP) photodegradation

20 mg of photocatalyst was dispersed in 50 mL of 0.066 mM APAP (10 mg.L^{-1}) aqueous solution by sonication for 5 min in the dark, and then transferred to a 250 mL glass photoreactor covered with a quartz plate and illuminated from above The reaction mixture was stirred for a further 30 min in dark to equilibrate any molecular adsorption. An aliquot of the reaction mixture was then collected (t_0) prior to visible light irradiation using a 500 W Xe lamp with a 420 nm cut-off filter: solution temperature was maintained at 25° C and stirring at 500 rpm throughout. Light intensity at the catalyst was 1.82 mW/cm^2, over an effective irradiation area of 4.5 cm (distance from light source to the photoreactor centre was 14. 9 cm). Quantum efficiency calculations are detailed in the Supporting Information. Aliquots were periodically sampled and filtered using a CPO20AN, prior to HPLC analysis. APAP degradation was monitored using a JASCO LC-netII/ADC HPLC with UV-2075 (243 nm) detector and a Shodex C18M4E analytical column (4.6 mm I.D × 250 mm) held at 25 °C, with pressure minimum and maximum of 0.2 MPa and 20 MPa respectively, and a mobile phase of 30:70 (v/v) acetonitrile:water with a flow rate of 0.6 mL/min. APAP conversion was calculated according to **Eqn. 2**.

$$\text{APAP removal efficiency (\%)} = \frac{\text{APAP intial} - \text{APAP final}}{APAP\ initial} \times 100 \qquad (2)$$

where initial and final are the molar concentrations of N-acetyl-para-aminophenol in the t0 sample and at the end of reaction respectively. Reaction products were identified by HPLC calibration with reference compounds (benzoquinone, hydroquinone, and maleic, fumaric and oxalic acids) and LC-MS analysis on an Agilent 6545 LC/Q-TOF using a ZORBAX SB-C1" Rapid Resolution HD column (2.1 I.D. x 150 mm x 1.8 μm) at 25 °C with 95:5 (v/v) water:methanol (acidified with 0.1% HCOOH) and acetonitrile mobile phases using a gradient program ramping the acetonitrile co-feed from 5 to 100 % over 12 min.

2.5. Trapping experiments

Scavengers: 1 mmol of *p*-benzoquinone, isopropyl alcohol, or disodium ethylenediaminetetraacetic acid (EDTA) were added to a reaction mixture of 20 mg Cu_2O@CuO-B in 50 mL of 0.06 mM APAP aqueous solution, as trapping agents for superoxide radicals ($O_2^{\bullet-}$), hydroxyl radicals ($^{\bullet}OH$), and holes (h_{vb}^+) respectively. Visible light photocatalytic degradation of APAP was then performed as described above.

Hydroxyl radicals: Hydroxyl-mediated oxidation of terephthalic acid (TA) to 2-hydroxyterephthalic acid (HTA) was conducted by adding 0.9 mmol TA to an ultrasonicated mixture of 20 mg Cu_2O@CuO-B in 50 mL water, and then irradiated with visible light in the above quartz reactor. Aliquots (1 mL) of the reaction mixture were periodically sampled and HTA emission spectra measured using a JASCO F-6600 spectrofluorometer under 315 nm excitation. DMSO trapping of reactively-formed formaldehyde was performed by ultrasonicating 20 mg of Cu_2O with 50 mL of 250 μM DMSO followed by visible light irradiation in the above quartz reactor. Aliquots (1 mL) of the reaction mixture were periodically sampled and derivatised using 20μL H_3PO_4-NaH_2PO_4

buffer and 200µL of 240 µmol/L DNPH. The resulting DNPH-HCHO complexe was analysed using a JASCO LC-netII/ADC HPLC with UV-2075 (355 nm) detector and a Shodex C18M4E analytical column (4.6 mm I.D × 250 mm) held at 32.2 °C and 17.4 MPa, with a mobile phase of 60:40 (v/v) methanol:water and flow rate of 0.8 mL/min.

3. Results and discussion

The phase composition and crystallinity of Cu_2O@CuO materials was characterized by PXRD (**Fig. 1**). All samples were dominated by reflections characteristic of Cu_2O (JCPDS 01-078-2076). Cu_2O@CuO-B and Cu_2O@CuO-D also exhibited weak reflections for CuO (JCPDS 01-073-6372), while Cu_2O@CuO-A and Cu_2O@CuO-B exhibited weak reflections for $Cu_2(OH)Cl$ (JCPDS 01-087-0679), and fcc Cu metal (JCPDS 01-07-3038).[21, 37] Cu_2O@CuO-C only contained crystalline Cu_2O. Volume-averaged crystallite sizes for the Cu_2O phase calculated from the Scherrer equation varied between 12 and 52 nm (**Table 1**), being largest for Cu_2O@CuO-B (greatest hydrazine concentration) and Cu_2O@CuO-D (least PEG), possibly reflecting faster reduction kinetics (fewer Cu_2O nucleation centres) and less disruption of the nucleation network respectively. Metallic Cu nanoparticles were respectively ~12 and 15 nm diameter for Cu_2O@CuO-A and Cu_2O@CuO-D.

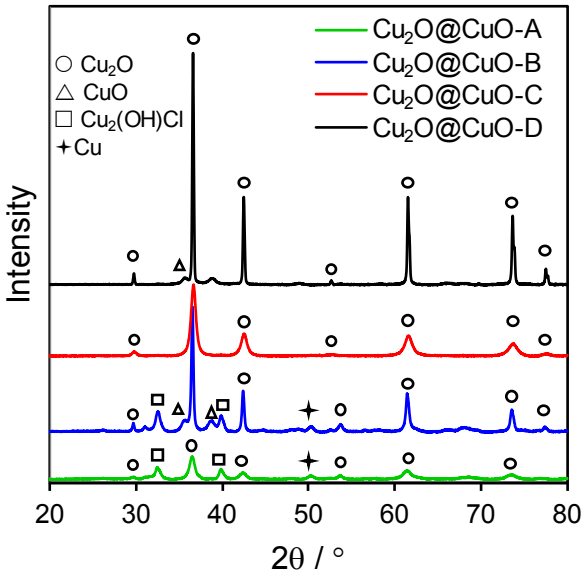

Fig. 1. Powder XRD patterns of Cu_2O@CuO.

The morphology of Cu_2O@CuO materials was subsequently explored by FE-SEM (**Fig. 2a-d** and **Fig. S1**). Addition of hydrazine before NaOH or use of 3 mL PEG resulted in 250-500 nm cauliflower aggregates, Cu_2O@CuO-A, Cu_2O@CuO-B and Cu_2O@CuO-C, whereas delayed addition of hydrazine and the use of a lower amount of PEG (0.5 mL) favoured larger and more uniform spherical structures with a textured surface, Cu_2O@CuO-D, indicating that the structure-directing agent strongly influenced overall nanostructure dimensions. The external appearance of these is similar to larger CuO/Cu_2O composite hollow microspheres prepared by high temperature (200 °C) hydrothermal ageing of an aqueous $Cu(CH_3COO)_2$ solution.[29] Nitrogen

View Article Online
DOI: 10.1039/C9TA07009E

porosimetry resulted in type II adsorption-desorption isotherms with small H3-type hysteresis loops (**Fig. S2**); there was no systematic variation in surface areas with synthesis protocol, which spanned 12-25 $m^2.g^{-1}$ (**Table 1**) comparable to hierarchical Cu_2O nanocubes[38] and CuO/Cu_2O hollow microspheres.[29]

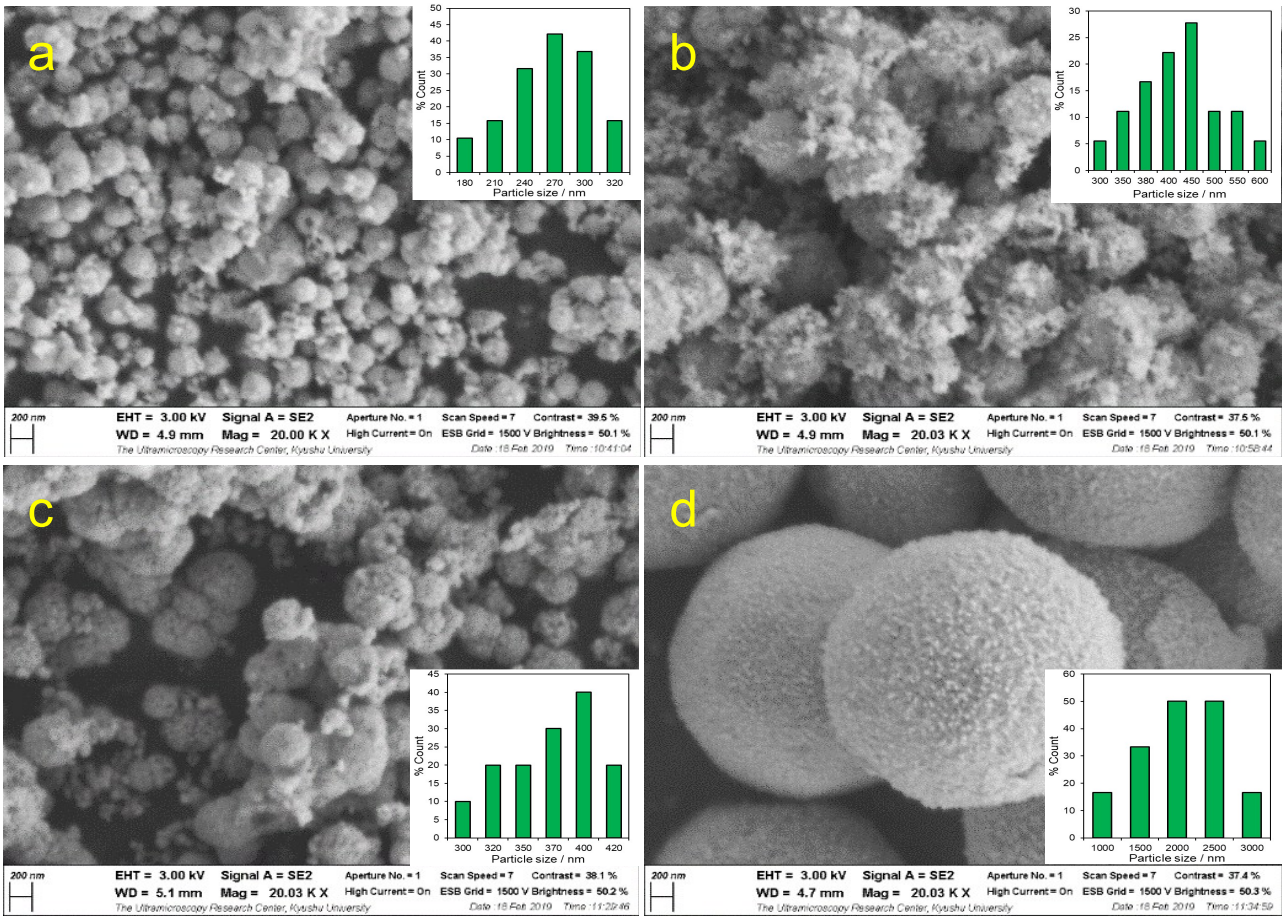

Fig. 2. FE-SEM images of (a) Cu_2O@CuO-A, (b) Cu_2O@CuO-B, (c) Cu_2O@CuO-C, (d) Cu_2O@CuO-D.

(S)TEM imaging provided more insight into the nature and internal architecture of the preceding nanostructures (**Fig. 3** and **Fig. S3**) formed by Ostwald ripening (and surface oxidation) of Cu_2O crystallites within the parent spherical aggregates.[39] Cu_2O@Cu_2O-A, Cu_2O@Cu_2O-B and Cu_2O@Cu_2O-C comprised spherical nanoparticles with differential contrast between the lighter core and denser shell regions (indicative of either a hollow or separated core, **Fig. 3a-d**). The cauliflower-like appearance of these three materials arises from small crystallites (likely Cu_2O or CuO, **Fig. 1**) that irregularly decorate the external shell. Cu_2O@Cu_2O-D also exhibits a core-shell structure, albeit with a denser core and lighter shell which we attribute to a dense polycrystalline interior resulting from the lower concentration of PEG in the synthesis and hence minimal disruption to the initial Cu_2O nuclei aggregation process (i.e. no intraparticle voids). Cu_2O@Cu_2O-A and Cu_2O@Cu_2O-C comprised hollow shells almost identical to those obtained by symmetric hollowing of Cu_2O spherical particles in the presence of polyvinylpyrrolidone (PVP).[39] In contrast, Cu_2O@Cu_2O-B exhibited a rattle-like core-shell structure (**Fig. 3b** and **Fig. S4a-c**) akin to that previously reported during the asymmetric hollowing of Cu_2O spherical particles in the presence of PEG,[39] attributed to inhomogeneous packing of primary Cu_2O crystallites in the spherical

View Article Online
DOI: 10.1039/C9TA07009E

aggregate formed on hydrazine reduction; subsequent Ostwald ripening was not initiated in the centre of the spherical aggregate resulting in a residual Cu_2O/Cu core. EDX mapping of Cu_2O@Cu_2O-B confirms a uniform distribution of Cu and O between different core-shell particles (**Fig. 3e-f**). Higher resolution images of Cu_2O@Cu_2O-B (**Fig. 3g** inset) revealed lattice fringes characteristic of CuO [(111) at 2.52 Å] in the corona of irregular crystallites, Cu_2O [(111) at 2.46 Å] in the main shell, and metallic copper [(200) at 1.81 Å) within the core,[9, 26, 40, 41] consistent with the phases observed by XRD. Quantitative EDX microanalysis across an individual rattle-like core-shell nanoparticles reveals an increase in the Cu:O stoichiometry from 1:1 in the corona to 1.43:1 in the centre of the core, consistent with a transition from a pure CuO exterior to a Cu_2O-like interior. Note that core analysis is complicated by contributions from the encapsulating shell, and hence the measured Cu:O stoichiometry does not reach 2:1 as anticipated for a 'naked' Cu_2O nanoparticle. The composition of core and shell regions was verified by spatially resolved electron energy loss spectroscopy (EELS), with the signatures for CuO and Cu_2O[42] identified in the respective corona and shell of Cu_2O@Cu_2O-B (**Fig. 3h-i**); note that copper metal does exhibit a detectable energy loss spectrum.[43, 44] Formation of a core-shell Cu_2O@CuO structure indicate that Cu_2O nanoparticles formed by hydrazine reduction of Cu(II) ions complexed within PEG micelles are kinetically-stabilised towards subsequent oxidation by a passivating CuO outer shell[45] (itself comprised on nanoparticle aggregates, possibly formed by an Ostwald ripening process mediated by the PEG[23, 39, 46]). Similar size (~400 nm) core-shell structures are reported by electrodeposition of $CuSO_4$ over a H-terminated p-type Si (100) substrate.[27]

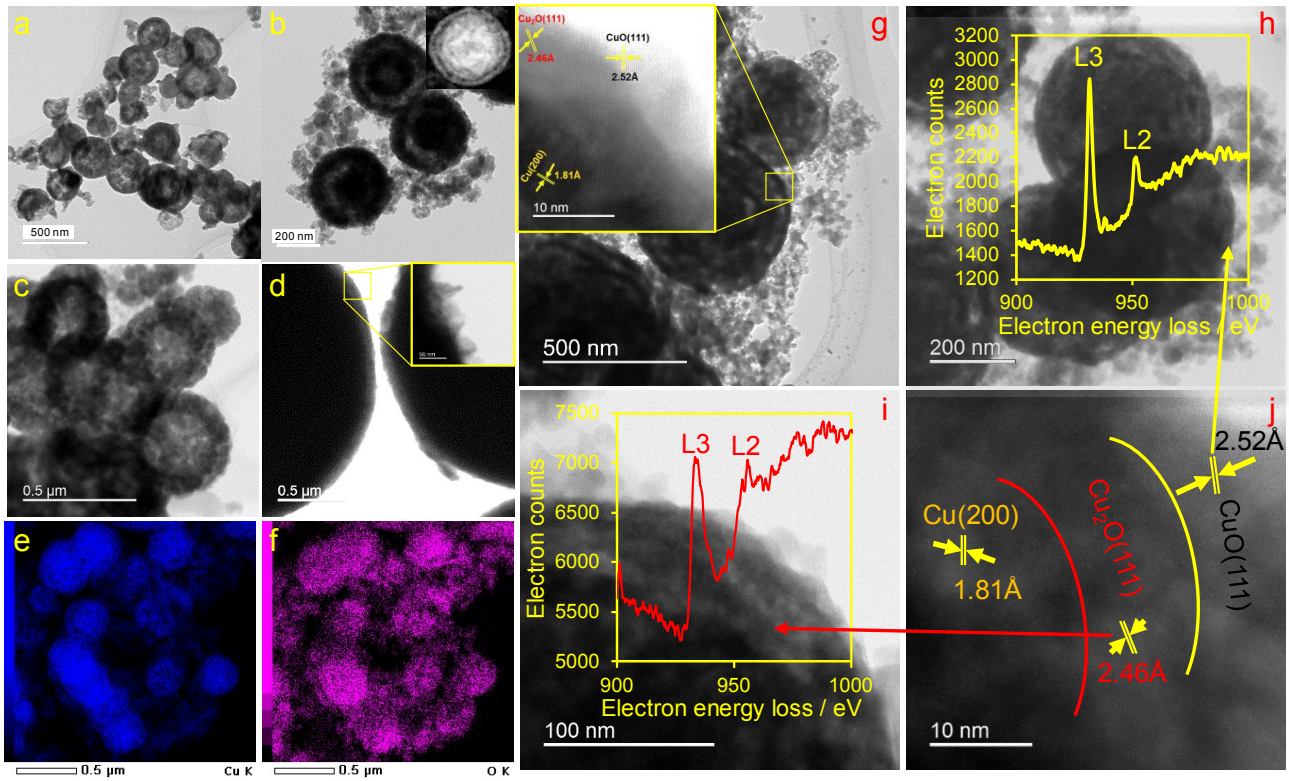

Fig. 3. Bright-field low resolution TEM images of (a) Cu_2O@CuO-A, (b) Cu_2O@CuO-B (inset STEM), (c) Cu_2O@CuO-C, (d) Cu_2O@CuO-D, and corresponding (e-f) EDX elemental maps, (g-j) high resolution TEM images, and (h-i) EELS spectra of Cu_2O@CuO-B.

View Article Online
DOI: 10.1039/C9TA07009E

The electronic and optical absorption properties of Cu_2O@CuO samples were determined by DRUVS (**Fig. 4**). All samples exhibited broad absorbances around 200-600 nm consistent with previous reports for copper oxides.[9, 24] CuO and Cu_2O are indirect and direct band gap semiconductors respectively.[47] Since CuO was present in all Cu_2O@CuO samples (see XAS fitting below) and exhibits a narrower energy gap than that of (direct band gap) Cu_2O, indirect band gaps were calculated from Tauc plots (**Fig. S5**) according to Eqn. (4):

$$\alpha h\nu = A(h\nu - E_g)^{\eta} \quad (4)$$

where A is absorption coefficient, α is linear absorption coefficient, h is Planck's constant, $h\nu$ is the photon energy, and Eg the band gap determined for α determined using the Kubelka-Munk formalism in Eqn. (5):

$$a = \frac{(1-R)^2}{2R} \quad (5)$$

Resulting indirect band gaps spanned 2.48 eV (Cu_2O@CuO-B) to 2.01eV (Cu_2O@CuO-D), similar values to those for hollow Cu_2O nanoshells (formed by PVP-mediated aggregation of nuclei into solid spheres in the initial reduction step of the synthesis). It is unlikely that this variation is due to quantum confinement effects, since these typically occur for sub-10 nm for Cu_2O nanoparticles,[24] i.e. smaller than any crystallites in our Cu_2O@CuO materials (**Table 1**), and is more likely due to morphology-dependent light absorption and scattering by Cu_2O (and CuO) nanoparticles.

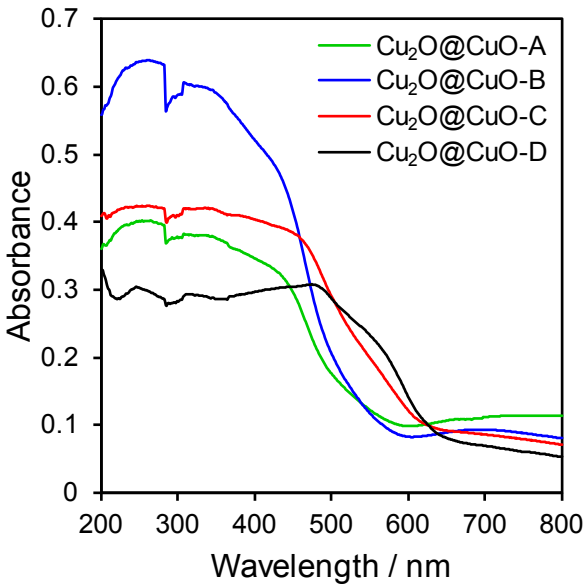

Fig. 4. DRUV spectra of Cu_2O@CuO.

View Article Online
DOI: 10.1039/C9TA07009E

Table 1. Physicochemical properties of Cu_2O@CuO.

Catalyst	Cu_2O crystallite size[a] / nm	Surface area[b] / $m^2.g^{-1}$	Band gap[c] / eV	VB edge potential[d] / eV	CB edge potential[d] / eV	Mean particle size[e] / nm
Cu_2O@CuO-A	11.8	25	2.43	1.55	-0.88	240-300
Cu_2O@CuO-B	37.1	21	2.48	1.57	-0.91	350-500
Cu_2O@CuO-C	13.1	18	2.25	1.33	-0.92	350-400
Cu_2O@CuO-D	52.0	12	2.00	1.24	-0.76	2700

[a]XRD; [b]N_2 porosimetry; [c]DRUVS; [d]Valence band XPS and DRUVS; [e]Cu 2p XPS. [f] TEM

The surface oxidation state of core-shell Cu_2O@CuO materials was also examined by XPS (**Fig. 5a**). Cu 2p XP spectra of all samples evidenced multiple chemical environments, with spin-orbit split core-level binding energies of 931.7±0.5 eV and 951.6±0.2 characteristic of Cu(I)/Cu(0) species, and shakeup satellites around of 940 eV and 960 eV indicative of Cu(II),[24] consistent with the observation of Cu_2O and CuO features by XRD (**Fig. 1**), TEM and EELS (**Fig. 3**). The Cu(II) satellite was weakest for Cu_2O@CuO-C, in accordance with XRD for which no crystalline CuO phase was detected (although this sample also exhibited the most clearly defined Cu(II) core-level photoemission ~933.5 eV), however for all materials the intensity of CuO features was greater than apparent from XRD (a bulk analytical method). This is in accordance with the core-shell structure visualised by TEM (**Fig. 3**) wherein a thin corona of CuO nanoparticles protects an underlying Cu_2O shell against oxidation, resulted in the CuO surface enrichment observed by XPS. Surface passivation of Cu_2O nanoparticles is also reported using organic ligands (3-mercaptopropionic acid).[40] Oxidation potentials for the Cu_2O@CuO materials were subsequently determined from valence band XPS measurements (**Fig. S6**). The valence band maximum (VBM) values were larger than reported for hierarchical nanocubes (~0.6 eV)[38] but smaller than those for single crystal Cu_2O films (2.09 eV),[48] and in all cases are significantly higher than that required to generate hydroxyl radicals (0.82 V versus NHE at pH 7). Corresponding conduction band maximum (CBM) values were approximately -0.9 eV, and hence sufficient to generate reactive oxygen species (-0.16 V at pH 7).[49] Cu K-edge XANES provided additional insight into the local chemical environment of copper species (**Fig. 5b**), with all materials exhibiting a rising-edge feature around 8982 eV and an intense white line around 8995 attributed to 1s→4pz (or 4px,ypz for Cu(I) species) and 1s→4p (continuum) transitions respectively. [50, 51] A very inflection was also observed around 8977 eV for Cu_2O@CuO-A and Cu_2O@CuO-B, attributed to the dipole-forbidden 1s→3d transition, pre-edge feature characteristic of Cu(II), and indeed the overall spectra for both resembled that of pure CuO. In contrast, the spectra of Cu_2O@CuO-C and Cu_2O@CuO-D closely resembled pure Cu_2O, exhibiting a pronounced 8981 eV rising-edge feature. Linear combination fitting to reference materials confirmed that Cu_2O@CuO-A and Cu_2O@CuO-B were predominantly comprised of CuO, while Cu_2O@CuO-C and Cu_2O@CuO-D were predominantly Cu_2O (**Table 2**). Note that the absence of detectable CuO for Cu_2O@CuO-A by XRD (**Fig. 1**) suggests that this phase must either be present as very small (<2 nm) crystallites or as amorphous particles, consistent with their location within the corona as observed by

View Article Online
DOI: 10.1039/C9TA07009E

XPS. Trace copper metal could also be fitted for Cu_2O@CuO-A and Cu_2O@CuO-B, in agreement with XRD and TEM for the latter material (**Fig. 3 g** and **j**).

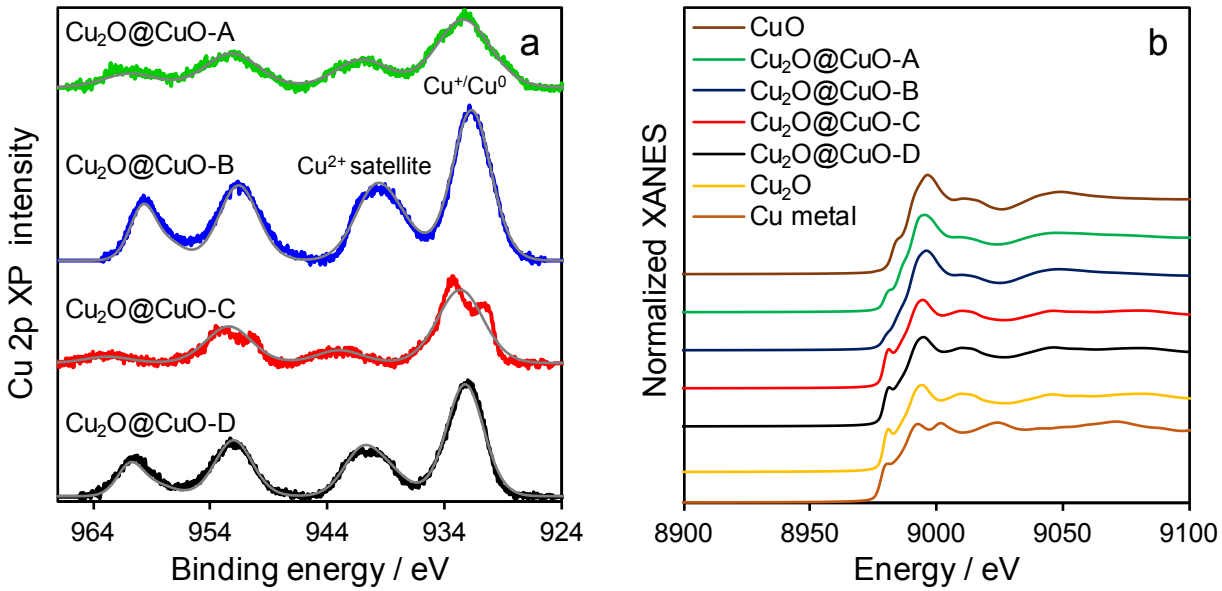

Fig. 5. (a) Cu 2p XP and (b) Cu K-edge XANES spectra of Cu_2O@CuO and reference materials.

Table 2. Linear combination fitting of Cu_2O@CuO XANES.

Catalyst	Cu_2O / %	CuO /%	Cu / %	Cu(I):Cu(II)	R-factor
Cu_2O@CuO-A	13.8	84.7	1.5	0.16	0.0030
Cu_2O@CuO-B	22.1	75.8	2.1	0.29	0.0042
Cu_2O@CuO-C	84. 6	15.4	-	5.49	0.0002
Cu_2O@CuO-D	81.3	18.7		4.34	0.0008

Photocatalytic APAP oxidation

Photocatalytic degradation of APAP under visible light irradiation was subsequently conducted using the preceding Cu_2O@CuO materials. APAP does not absorb visible light, and hence cannot act as a photosensitiser which is problematic in mechanistic investigations of e.g. photocatalytic dye degradation[30]. Negligible adsorption or reaction occurred over any Cu_2O@CuO material in the dark (<3.6 % APAP loss). Cu_2O@CuO-B was the most active towards APAP removal, achieving 48 % removal in 90 min, equating to an apparent quantum efficiency (AQE) of 8 % (**Fig. 6a-b**). Initial rates for APAP decomposition under visible light were 2.5, 7.0, 5.0 and 3.5×10^{-3} mmol.g^{-1}.min^{-1} for Cu_2O@CuO-A, Cu_2O@CuO-B, Cu_2O@CuO-C and Cu_2O@CuO-D respectively, (**Fig. 6c**) outperforming literature systems (**Table S1**), and quantitatively mirroring the trend in AQE values. The latter correlation suggests that the higher activity of Cu_2O@CuO-B must be associated with

View Article Online
DOI: 10.1039/C9TA07009E

either increased visible light absorption or improved charge carrier transport and/or lifetimes. Regarding the former, DRUVS measurements reveal Cu_2O@CuO-B possesses the widest band gap and hence will only be photoexcited by the smallest proportion of the incident spectrum, however light absorption and scattering is strongly dependent on particle morphology and shell thickness,[39, 52] with rattle-like core-shell mesoporous TiO_2 spheres outperforming hollow analogues for phenol degradation, attributed to increased absorption through internal light scattering.

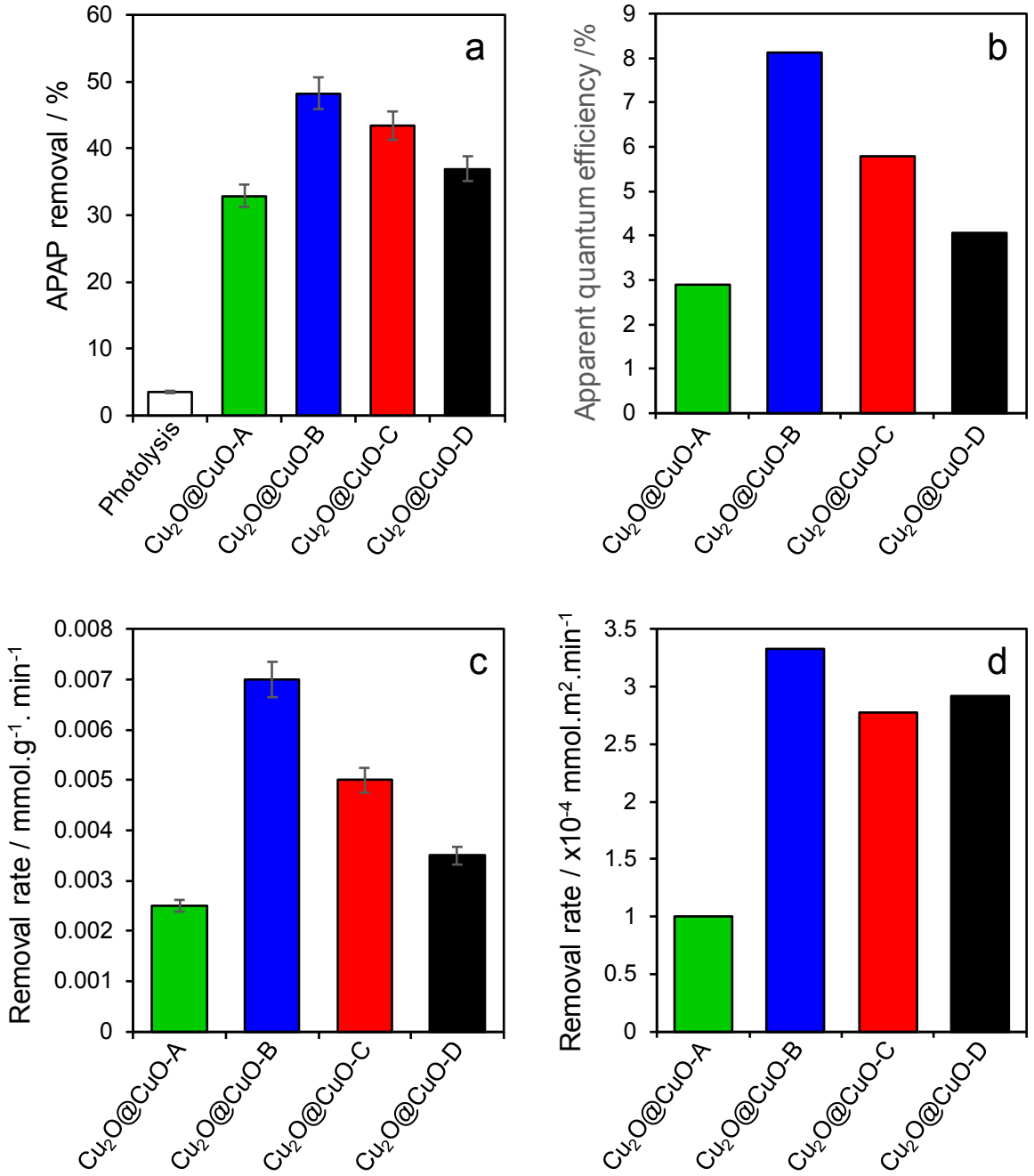

Fig. 6. (a) Removal efficiency, (b) apparent quantum efficiency, (c) specific activity, and (d) surface area normalised rate of APAP photocatalytic degradation over Cu_2O@CuO under visible light. Reaction conditions: 0.06 mmol APAP; 50 mL water; 20 mg catalyst; 300 min for (a-b) and 90 min for (c-d).

View Article Online
DOI: 10.1039/C9TA07009E

To investigate whether charge carrier lifetimes also differ between the Cu_2O@CuO photocatalysts, their steady state photoluminescence was compared under 380 nm and 560 nm excitation (**Fig. 7a-b**). Under both excitation sources Cu_2O@CuO-B exhibited the weakest emission at 420, 572 nm and 616 nm, consistent with slower radiative recombination of photoexcited electron-hole pairs, and hence longer charge carrier lifetimes.[38, 53, 54] The higher activity of Cu_2O@CuO-B for photocatalytic APAP degradation is thus likely associated with both increased light absorption due to strong scattering between the shell and rattle-like core, and suppressed charge recombination (due to transfer between Cu_2O and CuO/Cu).

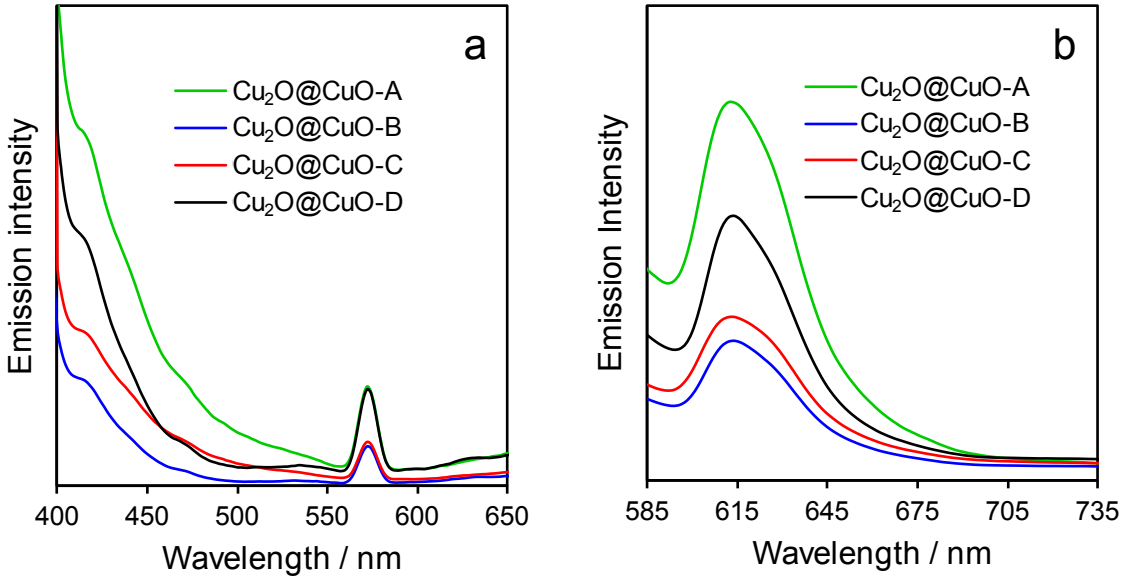

Fig. 7. Photoluminescence spectra of Cu_2O@CuO under (a) 380 nm excitation and (b) 560 nm excitation and emission. Excitation bandwidth 3 nm; emission bandwidth 10 nm, response 0.5 s, 900 V, 200 nm.min^{-1} scan.

By-products of APAP degradation over Cu_2O@CuO-B were determined by HPLC (**Fig. S7**), revealing the formation of aromatic hydroquinone and benzoquinone, and ring-opened fumaric, maleic, and oxalic acids (**Scheme 2**): preliminary LC-MS analysis confirmed hydroquinone as a reactive intermediate. Hydroxyl radicals ($^{\bullet}$OH) are proposed the active species responsible for photocatalytic APAP degradation over P25 TiO_2, with initial hydroxylation of the aromatic at the para (and ortho and meta) position with respect to the -OH to form hydroxyquinone, and subsequent $^{\bullet}$OH oxidation forming *p*-benzoquinone (BQ) which undergoes ring opening and further oxidation to produce maleic and other carboxylic acids.[55, 56]

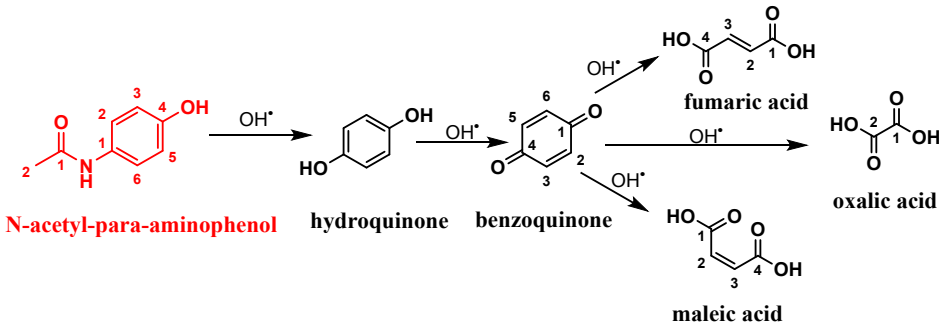

Scheme 2. Proposed reaction pathways in APAP photocatalytic degradation over Cu_2O@CuO-B.

The nature of the active species responsible for APAP photocatalytic degradation over Cu_2O@CuO-B was explored through additional experiments in the presence of either *p*-benzoquinone (BQ), isopropyl alcohol (IPA), or disodium ethylenediaminetetraacetic acid (EDTA), as trapping agents for superoxide radicals ($O_2^{\bullet-}$), hydroxyl radicals ($^{\bullet}OH$), and holes (h_{vb}^{+}) respectively (**Fig. 8a**). IPA addition had the greatest impact on the rate of APAP removal, causing it to decrease from 7×10^{-3} mmol.g^{-1}.min^{-1} to only 1.5×10^{-3} mmol.g^{-1}.min^{-1} mmol.g^{-1}.min^{-1}, a significantly lower rate than observed on the addition of either BQ or EDTA. This strongly suggests that $^{\bullet}OH$ species are responsible for APAP oxidation, as reported for titania photocatalysts.[34] Additional evidence for hydroxyl radical formation by Cu_2O@CuO-B was obtained undertaken through fluorescence spectroscopy. Briefly, an aqueous solution of terephthalic acid (TA) was irradiated in the presence of Cu_2O@CuO-B and the subsequent emission spectra monitored as a function of irradiation time: in the presence of $^{\bullet}OH$ radicals TA undergoes oxidation to 2-hydroxyterephthalic acid (HTA), which is characterised by a 425 nm emission (**Fig. 8b**). Continuous HTA formation was observed over the course of 300 min (the duration of APAP photocatalytic degradation experiments) confirming that Cu_2O@CuO-B is very active for $^{\bullet}OH$ radical production under visible irradiation. As final verification of the efficacy of Cu_2O@CuO-B for $^{\bullet}OH$ formation under visible light, formaldehyde (HCHO) production by DMSO trapping of hydroxyl radicals was demonstrated; a standard analytical method in advanced oxidation processes.[57] The resulting formaldehyde was derivatised with dinitrophenylhydrazine (DNPH), and evolution of the DNPH-HCHO complex followed by HPLC (**Fig. S8**).

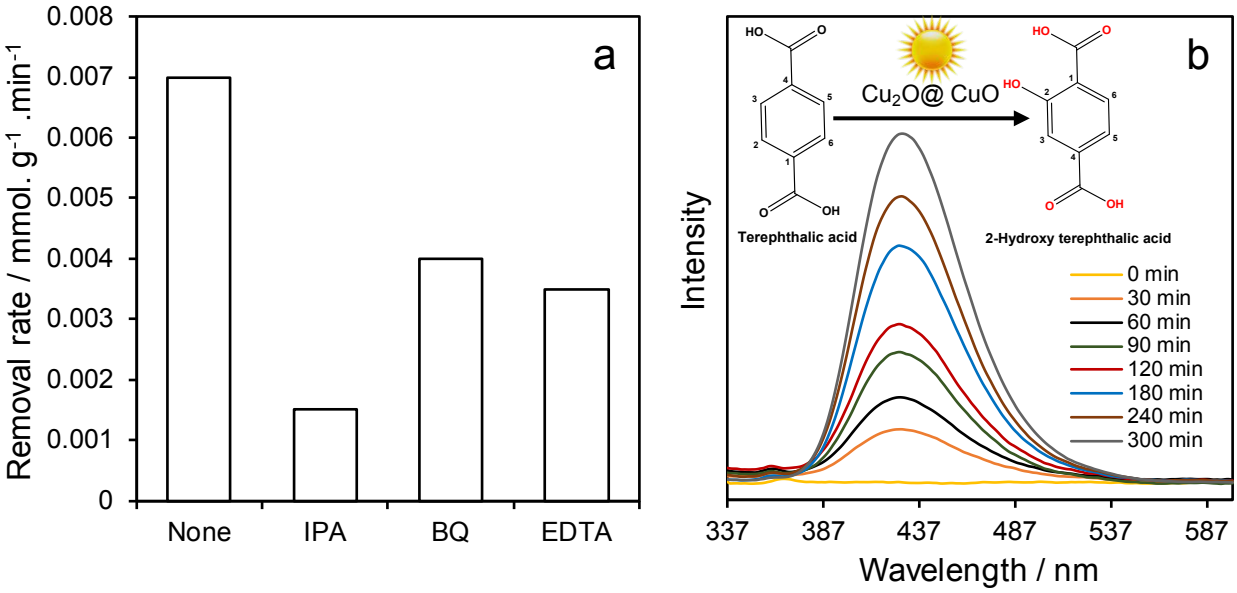

Fig. 8. (a) Influence of trapping agent addition on the rate of APAP removal over Cu_2O@CuO-B under visible light: 0.06 mmol APAP; 1 mmol scavenger; 50 mL water; 20 mg catalyst. (b) HTA emission spectra as a function of reaction time over Cu_2O@CuO-B under visible light: 0.9 mmol TA; 50 mL water; 20 mg catalyst; 315 nm excitation; excitation bandwidth 3 nm; emission bandwidth 10 nm, response 0.5 s, 900 V, 200 nm.min^{-1} scan.

View Article Online
DOI: 10.1039/C9TA07009E

Photocatalyst stability is critical for practical application, and hence was also investigated for the most active Cu_2O@CuO-B material. Negligible deactivation was observed over four consecutive cycles of APAP photodegradation under visible light (**Fig. S9**), consistent with the excellent physicochemical stability observed by SEM, XRD and XPS (**Fig. 9**); particle morphology, phase/crystallinity and oxidation state were unchanged even after 20 h continuous APAP photocatalytic degradation.

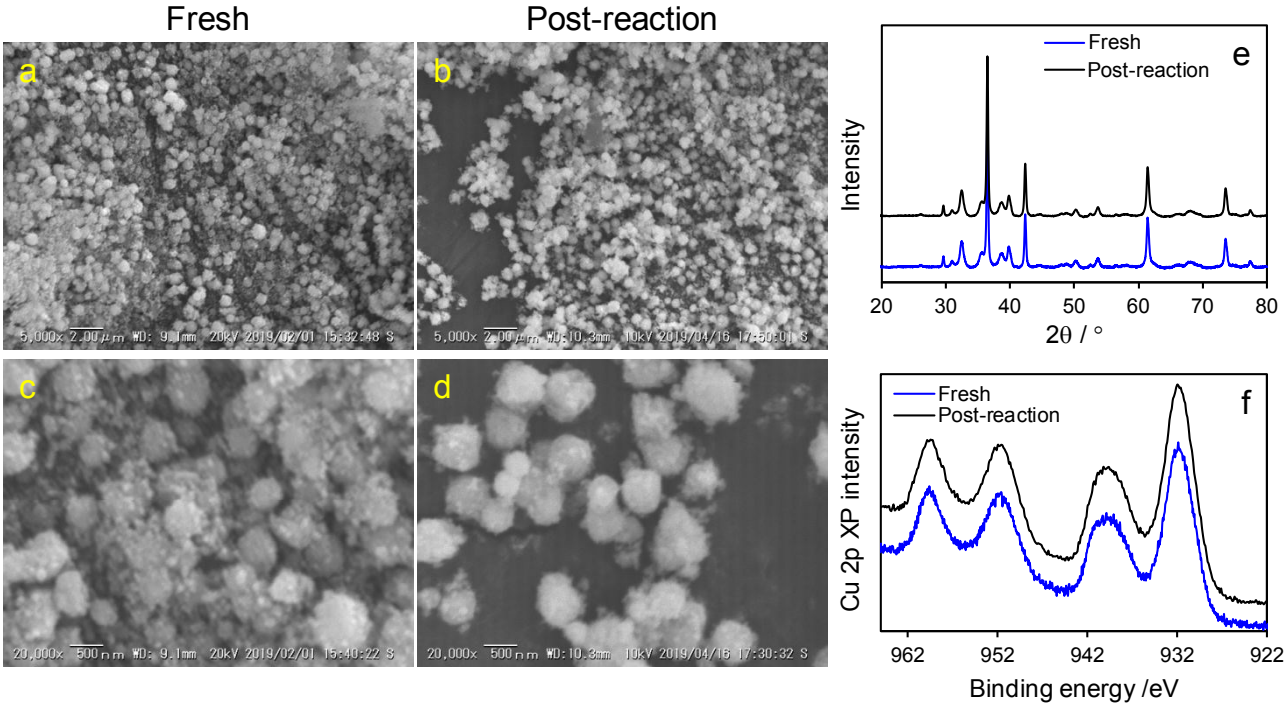

Fig. 9. (a-d) High and low magnification SEM, (e) XRD and (f) XPS of Cu_2O@CuO-B before and after 20 h APAP photocatalytic degradation.

3.1. Photocatalytic APAP removal Mechanism

Visible light photocatalytic APAP degradation over core-shell Cu_2O@CuO nanospheres is proposed to occur by e^- photoexcitation into the conduction band of the Cu_2O shell, and subsequent transfer across the heterojunction interface into the conduction band of the CuO corona.[24, 25, 47] These photoexcited e^- are sufficiently energetic (-0.8 to -0.9 eV) to reduce dissolved oxygen (O_2) and produce superoxide radical anions ($O^{2\bullet-}$) which in turn can react with water to form $^\bullet$OH radicals able to oxidise APAP (**Scheme S1**). Simultaneously, photoexcited h^- formed in the valence band of the CuO corona may inject across the heterojunction into the valence band of the Cu_2O shell, and subsequently reacted with hydroxyl ions to form additional $^\bullet$OH radicals. Charge separation across the Cu_2O/CuO interface suppresses bulk recombination of photogenerated e^--h^+ pairs, increasing charge carrier lifetimes and hence the probability of migration to the surfaces of both semiconductor nanoparticles of the nanosphere aggregates. The high activity and quantum efficiency of the Cu_2O@CuO-B photocatalyst is likely associated with a combination of factors. This material possesses the greatest oxidation and reduction potentials for $^\bullet$OH radical formation and exhibits the weakest photoluminescence. The latter is consistent with a high degree of photoexcited e^--h^+ separation and may reflect

View Article Online
DOI: 10.1039/C9TA07009E

electron trapping by Cu metal nanoparticles in contact with the Cu_2O shell; Chen et al reported that Cu played an important role in trapping electrons photoexcited into the Cu_2O conduction band, thereby promoting photocatalytic degradation of methylene blue.[58] Ongoing investigations aim to elucidate the relative importance of core-shell nanosphere morphology and composition to further enhance visible light absorption, charge separation and mobility, and ultimately photocatalytic efficiency for organic micropollutant degradation and solar fuels production.

4. Conclusions

A family of core-shell Cu_2O(Cu)@CuO visible light photocatalysts were synthesised by a template-free, mild hydrothermal route. The resulting nanosphere aggregates, formed by Ostwald ripening of Cu_2O nuclei, exhibited tunable dimensions spanning 200 nm to 2 μm, and well-defined shells of 10-50 nm Cu_2O nanoparticles decorated by a (protective) corona of CuO nanoparticles. Photophysical properties, notably band gaps, conduction and valence band edges, and photoluminescence, varied with nanosphere size and composition. High concentrations of hydrazine reductant and PEG structure-directing agent promoted asymmetric Ostwald ripening resulting in rattle-like Cu_2O/Cu metal cores, whereas lower concentrations resulted in hollow cores. All photocatalysts were active for the aqueous phase degradation of N-acetyl-para-aminophenol (APAP), even at concentrations of 10 $mg.L^{-1}$ far exceeding those encountered in wastewater streams. Trapping studies employing a variety of molecular scavengers provide strong evidence that $^{\bullet}OH$ radicals are responsible for APAP oxidation, consistent with the quinone and carboxylic acid by-product formation. Rattle-like core-shell Cu_2O/Cu@CuO exhibited the highest apparent quantum efficiency and activity for visible light photocatalytic degradation of APAP, and showed excellent structural and chemical stability over 20 h testing. These results highlight the potential of composite semiconductor photocatalysts using Earth abundant elements for environmental remediation and solar (photo)electrocatalytic energy conversion.

Conflicts of interest

The authors declare no conflict of interest.

Acknowledgments

S.K. and K.S. would like to thank the Japan Society for the Promotion of Science (JSPS) for providing postdoctoral fellowship for foreign researchers (P18387) and the research grand (KAKENHI JP18F18387). We thank Prof. Kuniyoshi Shimizu and Mr. Dedi Satria at Graduate School of Agriculture, Kyushu University for supporting LC-MS analysis. XANES measurements were performed at Kyushu University Beamline (SAGA-LS /BL06 with proposal No. 2019IK004). FE-SEM and HR(S)TEM performed at Ultra Microscopic Analysis Center at Kyushu University and X-ray photoelectron spectra were collected at Advanced Analytical Centre (Nanotechnology Platform), Kyushu University under the proposal No. S-18-KU-0043.

View Article Online
DOI: 10.1039/C9TA07009E

References

1. F. Opoku, K. K. Govender, C. G. C. E. van Sittert and P. P. Govender, *Advanced Sustainable Systems*, 2017, **1**, 1700006.
2. D. Chen, X. Zhang and A. F. Lee, *Journal of Materials Chemistry A*, 2015, **3**, 14487-14516.
3. R. Ciriminna, R. Delisi, Y.-J. Xu and M. Pagliaro, *Organic Process Research & Development*, 2016, **20**, 403-408.
4. D. Friedmann, A. Hakki, H. Kim, W. Choi and D. Bahnemann, *Green Chemistry*, 2016, **18**, 5391-5411.
5. A. Fujishima, T. N. Rao and D. A. Tryk, *Journal of Photochemistry and Photobiology C: Photochemistry Reviews*, 2000, **1**, 1-21.
6. S. M. Gupta and M. Tripathi, *Chinese Science Bulletin*, 2011, **56**, 1639.
7. W.-K. Jo, S. Kumar, M. A. Isaacs, A. F. Lee and S. Karthikeyan, *Applied Catalysis B: Environmental*, 2017, **201**, 159-168.
8. M. B. Gawande, A. Goswami, F.-X. Felpin, T. Asefa, X. Huang, R. Silva, X. Zou, R. Zboril and R. S. Varma, *Chemical Reviews*, 2016, **116**, 3722-3811.
9. S. Karthikeyan, S. Kumar, L. J. Durndell, M. A. Isaacs, C. M. A. Parlett, B. Coulson, R. E. Douthwaite, Z. Jiang, K. Wilson and A. F. Lee, *ChemCatChem*, 2018, **10**, 3554-3563.
10. M. J. Siegfried and K. S. Choi, *Angewandte Chemie International Edition*, 2005, **44**, 3218-3223.
11. W.-C. Huang, L.-M. Lyu, Y.-C. Yang and M. H. Huang, *Journal of the American Chemical Society*, 2012, **134**, 1261-1267.
12. Y. Kwon, A. Soon, H. Han and H. Lee, *Journal of Materials Chemistry A*, 2015, **3**, 156-162.
13. Y. Liu, B. Zhang, L. Luo, X. Chen, Z. Wang, E. Wu, D. Su and W. Huang, *Angewandte Chemie International Edition*, 2015, **54**, 15260-15265.
14. F. Wang, W. Septina, A. Chemseddine, F. F. Abdi, D. Friedrich, P. Bogdanoff, R. van de Krol, S. D. Tilley and S. P. Berglund, *Journal of the American Chemical Society*, 2017, **139**, 15094-15103.
15. Y. Su, H. Li, H. Ma, H. Wang, J. Robertson and A. Nathan, *ACS Omega*, 2018, **3**, 1939-1945.
16. R. Chen, S. Pang, H. An, J. Zhu, S. Ye, Y. Gao, F. Fan and C. Li, *Nature Energy*, 2018, **3**, 655-663.
17. Y. Yang, D. Xu, Q. Wu and P. Diao, *Scientific Reports*, 2016, **6**, 35158.
18. Y. Zhu, Z. Xu, K. Yan, H. Zhao and J. Zhang, *ACS Applied Materials & Interfaces*, 2017, **9**, 40452-40460.
19. A. A. Dubale, C.-J. Pan, A. G. Tamirat, H.-M. Chen, W.-N. Su, C.-H. Chen, J. Rick, D. W. Ayele, B. A. Aragaw, J.-F. Lee, Y.-W. Yang and B.-J. Hwang, *Journal of Materials Chemistry A*, 2015, **3**, 12482-12499.
20. Z. Ai, L. Zhang, S. Lee and W. Ho, *The Journal of Physical Chemistry C*, 2009, **113**, 20896-20902.
21. J. Kou, A. Saha, C. Bennett-Stamper and R. S. Varma, *Chemical Communications*, 2012, **48**, 5862-5864.
22. C. C. Yec and H. C. Zeng, *Chemistry of Materials*, 2012, **24**, 1917-1929.
23. H. Xu and W. Wang, *Angewandte Chemie*, 2007, **119**, 1511-1514.
24. M. Yin, C.-K. Wu, Y. Lou, C. Burda, J. T. Koberstein, Y. Zhu and S. O'Brien, *Journal of the American Chemical Society*, 2005, **127**, 9506-9511.
25. H. Li, Z. Su, S. Hu and Y. Yan, *Applied Catalysis B: Environmental*, 2017, **207**, 134-142.
26. W. Chen, Z. Fan and Z. Lai, *Journal of Materials Chemistry A*, 2013, **1**, 13862-13868.
27. A. Radi, D. Pradhan, Y. Sohn and K. T. Leung, *ACS Nano*, 2010, **4**, 1553-1560.
28. J. J. Teo, Y. Chang and H. C. Zeng, *Langmuir*, 2006, **22**, 7369-7377.
29. H. Yu, J. Yu, S. Liu and S. Mann, *Chemistry of Materials*, 2007, **19**, 4327-4334.
30. N. Barbero and D. Vione, *Journal*, 2016.
31. S. Kumar, C. M. A. Parlett, M. A. Isaacs, D. V. Jowett, R. E. Douthwaite, M. C. R. Cockett and A. F. Lee, *Applied Catalysis B: Environmental*, 2016, **189**, 226-232.
32. J. Żur, A. Piński, A. Marchlewicz, K. Hupert-Kocurek, D. Wojcieszyńska and U. Guzik, *Environmental Science and Pollution Research*, 2018, **25**, 21498-21524.
33. T. Azuma, N. Arima, A. Tsukada, S. Hirami, R. Matsuoka, R. Moriwake, H. Ishiuchi, T. Inoyama, Y. Teranishi, M. Yamaoka, Y. Mino, T. Hayashi, Y. Fujita and M. Masada, *Science of The Total Environment*, 2016, **548-549**, 189-197.
34. L. Yang, L. E. Yu and M. B. Ray, *Environmental Science & Technology*, 2009, **43**, 460-465.

35. M. Skoumal, P.-L. Cabot, F. Centellas, C. Arias, R. M. Rodríguez, J. A. Garrido and E. Brillas, *Applied Catalysis B: Environmental*, 2006, **66**, 228-240.
36. S. D. Kim, J. Cho, I. S. Kim, B. J. Vanderford and S. A. Snyder, *Water research*, 2007, **41**, 1013-1021.
37. Q. Song, W. Liu, C. D. Bohn, R. N. Harper, E. Sivaniah, S. A. Scott and J. S. Dennis, *Energy & Environmental Science*, 2013, **6**, 288-298.
38. S. Kumar, M. A. Isaacs, R. Trofimovaite, L. Durndell, C. M. Parlett, R. E. Douthwaite, B. Coulson, M. C. Cockett, K. Wilson and A. F. Lee, *Applied Catalysis B: Environmental*, 2017, **209**, 394-404.
39. L. Zhang and H. Wang, *ACS Nano*, 2011, **5**, 3257-3267.
40. H. Azimi, S. Kuhri, A. Osvet, G. Matt, L. S. Khanzada, M. Lemmer, N. A. Luechinger, M. I. Larsson, E. Zeira, D. M. Guldi and C. J. Brabec, *Journal of the American Chemical Society*, 2014, **136**, 7233-7236.
41. S. B. Kalidindi, U. Sanyal and B. R. Jagirdar, *Physical Chemistry Chemical Physics*, 2008, **10**, 5870-5874.
42. L. Chen, S. Shet, H. Tang, H. Wang, T. Deutsch, Y. Yan, J. Turner and M. Al-Jassim, *Journal of Materials Chemistry*, 2010, **20**, 6962-6967.
43. N. J. Long and A. K. Petford-Long, *Ultramicroscopy*, 1986, **20**, 151-159.
44. R. D. Leapman, L. A. Grunes and P. L. Fejes, *Physical Review B*, 1982, **26**, 614-635.
45. V. R. Palkar, P. Ayyub, S. Chattopadhyay and M. Multani, *Physical Review B*, 1996, **53**, 2167-2170.
46. X. Meng, G. Tian, Y. Chen, Y. Qu, J. Zhou, K. Pan, W. Zhou, G. Zhang and H. Fu, *RSC Advances*, 2012, **2**, 2875-2881.
47. M. Heinemann, B. Eifert and C. Heiliger, *Physical Review B*, 2013, **87**, 115111.
48. X. Wang, D. Yan, C. Shen, Y. Wang, W. Wu, W. Li, Z. Jiang, H. Lei, M. Zhou and Y. Tang, *Opt. Mater. Express*, 2013, **3**, 1974-1985.
49. J. Li, M. Jiang, H. Zhou, P. Jin, K. M. C. Cheung, P. K. Chu and K. W. K. Yeung, *Global Challenges*, 2019, **3**, 1800058.
50. I. J. Drake, K. L. Fujdala, S. Baxamusa, A. T. Bell and T. D. Tilley, *The Journal of Physical Chemistry B*, 2004, **108**, 18421-18434.
51. A. Sharma, M. Varshney, J. Park, T.-K. Ha, K.-H. Chae and H.-J. Shin, *RSC Advances*, 2015, **5**, 21762-21771.
52. M. Xiao, Z. Wang, M. Lyu, B. Luo, S. Wang, G. Liu, H.-M. Cheng and L. Wang, *Advanced Materials*, **0**, 1801369.
53. I. Mukherjee, S. Chatterjee and N. A. Kulkarni, *The Journal of Physical Chemistry C*, 2016, **120**, 1077-1082.
54. A. Gómez-Avilés, M. Peñas-Garzón, J. Bedia, D. D. Dionysiou, J. J. Rodríguez and C. Belver, *Applied Catalysis B: Environmental*, 2019, DOI: https://doi.org/10.1016/j.apcatb.2019.04.040.
55. L. Yang, E. Y. Liya and M. B. Ray, *Water research*, 2008, **42**, 3480-3488.
56. D. Vogna, R. Marotta, A. Napolitano and M. d'Ischia, *The Journal of Organic Chemistry*, 2002, **67**, 6143-6151.
57. C. Tai, J.-F. Peng, J.-F. Liu, G.-B. Jiang and H. Zou, *Analytica Chimica Acta*, 2004, **527**, 73-80.
58. W. Chen, Z. Fan and Z. Lai, *Journal of Materials Chemistry A*, 2013, **1**, 13862-13868.

View Article Online
DOI: 10.1039/C9TA07009E